Journal of Materials Chemistry A

Particle Size Effect of Graphite Anodes on Performance of Fast Charging Li-Ion Batteries

Journal:	*Journal of Materials Chemistry A*
Manuscript ID	TA-ART-02-2023-000608.R3
Article Type:	Paper
Date Submitted by the Author:	15-Aug-2023
Complete List of Authors:	Wang, Guanyi; Western Michigan University Mijailovic, Aleksandar; Brown University Yang, Jian; Western Michigan University Xiong, Jie; Western Michigan University, Chemical and Paper Engineering Beasley, Sarah; Western Michigan University, Chemical and Paper Engineering Mathew, Kevin; Western Michigan University Zhou, Bingyao; Western Michigan University, Chemical and Paper Engineering Lu, Wenquan; Argonne National Laboratory, Sheldon, Brian; Brown University, Engineering Wu, Qingliu; Western Michigan University,

Particle Size Effect of Graphite Anodes on Performance of Fast Charging Li-Ion Batteries

Guanyi Wang[a], Aleksandar Mijailovic[b], Jian Yang[a], Jie Xiong[a], Sarah E Beasley[a], Kevin Mathew[a], Bingyao Zhou[a], Wenquan Lu[c,*], Brian W. Sheldon[b,*], Qingliu Wu[a,*]

a- Department of Chemical and Paper Engineering, Western Michigan University, 4601 Campus Drive, Kalamazoo, Michigan, 49008-5462, U. S.A.

b- School of Engineering, Brown University, 184 Hope St., Providence, Rhode Island, 02912, U. S. A.

c- Chemical Science and Engineering Division, Argonne National Laboratory, 9700 South Cass Ave., Lemont, Illinois, 60439-4837, U. S. A.

* Correspondence should be addressed to:

Wenquan Lu; email: wenquan.lu@anl.gov; Phone: 630-252-3704, Fax: 630-252-4176

Brian W. Sheldon; email: brian_sheldon@brown.edu; Phone: 401-863-2866

Qingliu Wu, email: qingliu.wu@wmich.edu; Phone: 269-276-3998; Fax: 269-276-3501

Abstract

Charging energy-dense lithium-ion batteries (LIBs) with thick graphite electrodes at high current densities are typically accompanied by poor performance and safety issues. The root cause is the onset of Li plating at the surface of graphite when lithiated to a high capacity within a short time period. Here, we investigated the behavior of graphite electrodes with various particle sizes under fast charge operations. Results from the electrochemical characterization on graphite electrodes exhibit the superiority of smaller particles over bigger particles in terms of suppressing the onset of Li plating and growth of plated Li particles. Observations from scanning electron microscopy also corroborate the presence of plated Li in electrodes with big graphite particles and its absence in graphite electrodes with small particles, when the cells were lithiated to 90% of the state of charge (SOC). The improved performance of cells with the small particles might be associated with the low Li-ion concentration at the surface of graphite and thus reduced overpotential in graphite electrodes. The simulated results revealed that, compared to bigger particles, smaller particles have lower surface intercalation at any given cell SOC, which may significantly reduce the overpotential in the graphite electrodes and mitigate the onset of Li plating. This agrees well with experimental observations.

Keywords: Graphite, Particle Size, Fast charging, Li-Ion Batteries

1. Introduction

With the premises of low cost, long cycle life, and acceptable capacity, graphite has predominated the market of negative electrodes in the state-of-the-art (SOA) lithium-ion batteries (LIBs) for electric vehicles (EVs) [1-3]. However, charging conventional thick graphite electrodes in energy-dense LIBs at high current densities generally results in detrimental performance and safety issues [4-6]. The major cause for this obstacle is Li plating, an undesired side reaction in which Li^+ ions are reduced to metallic Li instead of intercalating into the crystal structure of graphite [6-9]. Li plating can thermodynamically occur when the anode potential prematurely reaches 0 V (vs. Li^+/Li) at a given location [10, 11], and cause irreversible lithium loss, rapid capacity fade, electrolyte decomposition, internal micro-short and other deleterious effects [5, 12]. This plating onset might be the result of concentration polarization, kinetic overpotential and ohmic voltage drop [4, 6, 7, 9, 13]. Therefore, insights into the influences of physical/chemical battery parameters on the overpotential components will be of both scientific and practical significances in the development of fast charging LIBs. Here, we elucidate the effect of the particle size on mitigating the Li plating and growth of plated Li particles occurred in thick electrodes through both experiment and theoretical simulation to guide the manufacturing of graphite products and their selection for anodes in LIBs aiming at fast charge applications.

Facilitating the ionic and electronic transports across the electrodes is a prevalent strategy to alleviate Li plating in the graphite anodes. One major cause of the overpotential is associated with the sluggish Li^+ ion diffusion in the electrolyte [4, 7]. Especially at high rates, the fast depletion and

retardant transport of Li^+ ions in the liquid electrolyte phase within the electrode will build a large Li^+ ion concentration gradient across the electrode, and thus lead to high electrolyte concentration and ohmic overpotentials [6, 14, 15]. The introduction of gradient porosity features [16-18] or a secondary porous network (SPN) with pore channels perpendicular to the current collector [19-24] can significantly improve the Li-ion transport across graphite electrodes, and has been shown to successfully improve the rate capability of cells. Using electrolytes with high ionic conductivity can also effectively reduce the electrolyte concentration gradient and ohmic overpotential [4, 6, 9, 25, 26]. Another major cause of overpotential is related to the sluggish charge-transfer kinetics [7, 27, 28]. The charge-transfer process at the graphite electrodes involves the de-solvation of Li ions, diffusion of naked Li ions through the solid electrolyte interface (SEI), electron reception of Li ions at the SEI/graphite interface and diffusion of solid-state Li in the graphite phase [7, 8, 27]. Therefore, favoring the Li-ion transport in the solid-state phases can effectively reduce the kinetic overpotential in the graphite electrodes. For instance, surficial coating [29-32] and acid/base treatment [33] have been demonstrated to provide more accessible sites at the surface of graphite particles, effectively facilitate Li-ion transport, and consequently improve the rate capability of cells. Therefore, Li plating can be alleviated through accelerating the Li-ion transport in either liquid or solid, or both phases in the graphite electrodes.

The intercalation into the graphite electrode is a complex process and Li plating is a result of the combination of various factors. Most recently, our computation work suggests that reaction inhomogeneity, which is originated from the interplay of concentration gradient overpotential,

kinetic overpotential and ohmic overpotential, can lead to accelerated plating in the graphite electrodes at high charge rates[34, 35]. In that study, a small particle size was used to ensure even intercalation through particle thicknesses and limitations due to particle-level intercalation gradients was not studied. In fact, the intercalation rate also strongly depends on the morphology, particle size and particle size distribution of graphite. With a higher proportion of edge sites accessible to the electrolyte, briquette-like graphite has a relatively higher rate capability than that of spherical graphite [36]. Similarly, graphite with smaller particles [37-39] and a narrow particle size distribution exhibits a higher rate of intercalation [40]. However, reports from these researchers focused on understanding the relationship between intercalation kinetics and the graphite properties at relatively slow rates and with no heed to the dependence of Li plating on the particle size, especially at high rates.

Here, we use graphite powders with different average particle sizes as anodes of LIBs. The effect of particle size on the electrochemical behavior of graphite electrodes will be investigated, especially at high rates. The effect of the small particles on mitigating the Li plating onset and suppressing the growth of plated Li particles in the graphite electrodes will be demonstrated. The underlying mechanism will be elucidated.

2. Experimental

2.1. Material and Electrode Preparation

Four graphite powders, M3 (Hitachi MAGE3, D_{50} of 24.1 μm and D_{90} of 50.2 μm), P5 (Phillips 66, D_{50} of 6.5 μm and D_{90} of 12.2 μm), P10 (Phillips 66, D_{50} of 9.6 μm and D_{90} of 19.3

μm) and P15 (Phillips 66, D_{50} of 14.6 μm and D_{90} of 35.3 μm), were studied here. All graphite powders, carbon black (C45, Timcal) and polyvinylidene difluoride (PVDF, Solvay 9300) were used as received without further modification.

To prepare slurries, graphite and carbon black powders were dispersed in a PVDF solution dissolved in *N*-methyl-2-pyrrolidone (NMP). The homogenous slurry was obtained by using a mixer (AR-100, Thinky) and then hand casted onto the Cu foil. The electrode coatings were dried at 40 °C for 2 hours followed by additional drying at 80 °C under vacuum overnight. The dried electrodes were calendered to targeted thicknesses and kept for further applications and characterizations. All dried electrodes were composed of 92 wt.% graphite, 2 wt.% carbon black and 6 wt.% PVDF, densified to the same porosity of ~35%, and had an active material mass loading of ~ 7.5 mg/cm^2.

2.2. Characterizations

Crystal phase: The X-Ray Diffraction (XRD) analysis was performed on a diffractor (SmartLab SE, Rigaku) with a Cu Kα (λ=1.54 Å) in 2θ range of 10° - 90° at room temperature, and scan speed as 1 °/minute to reveal the crystal phase of the graphite powders.

Morphology: The structural information of graphite powders and electrodes was collected on a scanning electron microscope (SEM, JEOL JSM-IT200LA) with an accelerating voltage of 20 kV. Before SEM observations, the cycled electrodes were disassembled inside a glovebox and washed by ethyl methyl carbonate (EMC, TCI America). The harvested electrodes were then dried inside a glovebox overnight for further characterization.

Surface area and pore size distribution: A Tristar 3000 (Micromeritics Instrument Corporation) automatic gas sorption analyzer was used to determine the porous structure. The specific surface area (SSA) of different graphite samples were calculated from the nitrogen adsorption isotherms using the Brunauer-Emmett-Teller (BET) method.

Particle size distribution: The MIE scattering model was used to calculate the particle size distributions from diffraction data measured using a Malvern Panalytical Mastersizer 3000 diffractometer with a Hydro MV dispersion unit. This technique passes both 633 nm and 470 nm wavelength light sources through suspensions of graphite in toluene, with suspended solids concentration of 0.02 vol%. The light obscuration utilized for these measurements was 10%.

2.3. Electrochemical Measurements

Cell assembly: The dried electrodes were cut into discs with a diameter of 14 mm and assembled into CR-2032 coin cells with lithium metal as counter electrodes. A solution containing 1.2 M $LiPF_6$ dissolved in ethylene carbonate (EC)/ ethyl methyl carbonate (EMC) (3/7, w/w) was used as the electrolyte. The same procedure was used to assemble symmetrical cells with graphite electrodes as both cathode and anode. All cells were assembled inside a glovebox filled with Argon.

Formation: Galvanostatic cycling tests of assembled cells were conducted on a Neware CT-4008T battery tester at a constant current of C/10 over the voltage range of 0.01-1.5 V at room temperature. All cells underwent three formation cycles and then were divided into four groups for further characterizations.

Rate capability: After three formation cycles, the rate capability test was conducted on the

first group of cells by using a constant current-constant voltage (CC-CV) mode for both charge (delithiation) and discharge (lithiation) processes. A constant current of C/3 was used to delithiate the cells to 1.5 V, followed by a voltage hold at 1.5 V until the current fell below C/20 or the total delithiation time reached 3 hours and then rested 30 minutes before the next lithiation cycle. An incremental current density (C/10, C/2, 1C, 2C and 4C) was applied to the lithiation processes. At every rate, the cells were lithiated to 0.01 V with a constant current density followed by a voltage hold at 0.01 V until current density fell below C/20, or alternatively until the overall lithiation time reached the time corresponding to the rate, then rested 30 minutes before the next delithiation cycle. At every rate, the cells underwent three cycles.

Open-circuit voltage (OCV) and differential open-circuit voltage (dOCV) analysis: The second and third cell groups were used for OCV/dOCV study, which has been proven to be a promising method for detecting the Li plating onset [41-44]. After formation tests, the cells were lithiated to target state-of-charge (SOC) statuses, varied from 65% to 90% with an increment of 5% at 2C. After lithiated to each SOC, the cells rested for 30 minutes (OCV or relaxation period), delithiated to 1.5V with a constant current density of C/3, and rested for another 30 minutes before the next cycle, shown in **Figure S1**. The relaxation voltage data (OCV data) were collected at every 0.5s, shown in **Figure S2**, and the derivatives of the relaxation voltage (dOCV) were shown in **Figure S3**. To reduce significant noise in the dOCV, the same procedure and MATLAB smoothdata() function reported by Zachary and et al. [43] were used and the effect of data smoothing on the dOCV is illustrated in **Figure S4**. The same procedure was applied to the third cell group

with the rate of 4C applied to the lithiation, and OCV/dOCV data were shown in **Figure S5** and **S6**.

Long-term cycling tests at 4C: After the formation tests, the cycling tests were conducted on the fourth group of cells under the constant current (CC) mode: the cells were lithiated to 80% SOC at 4C, rested for 30 minutes, delithiated to 1.5V at C/3 and rested for another 30 minutes before next cycle.

Electrochemical impedance spectroscopy (*EIS):* After the formation tests, EIS data were collected on cells lithiated to 50% SOC at room temperature by using an impedance/gain-phase analyzer (Gamry Interface 1010E) with a potential amplitude of 5 mV in the frequency range of 0.05 Hz to 1.6 MHz. The same approach was applied to the symmetrical cells, and the tortuosity (τ) of the graphite electrodes was calculated using the equation below [45, 46]:

$$\tau = \frac{R_{ion} \times A \times k \times \varepsilon}{2d} \qquad (1)$$

Where A, d, ε, k, and R_{ion} are the electrode area (1.54 cm^2), electrode thickness (55-59 μm), electrode porosity (35%), electrolyte conductivity (9×10^{-3} S/cm for 1.2 M $LiPF_6$ in EC/EMC [47]) and ionic resistance, respectively. The ionic resistance (R_{ion}) was calculated using equation below [45, 46]:

$$R_{total} = \frac{R_{ion}}{3} + R_{contact} \quad (2)$$

R_{total} represents the total resistance and can be obtained through extrapolation of low-frequency tail data to intersect real axis, while $R_{contact}$ is the contact resistance and intercept of the

EIS curve with the real axis (**Figure S7**). The resistances of different graphite electrodes are summarized in **Table S1**. The collected data were used as inputs into the models below.

2.4. Modeling

The pseudo-2D model (P2D model) in COMSOL Multiphysics® 5.4 software, originally developed by Newman and coworkers, was used to model the effects of graphite particle size on lithium plating onset during fast charging. Most of the parameters used herein were used previously to model the same P5 graphite described herein[34, 35]. In the present study, the measured equilibrium potential (E_{eq}) for P5 was used for all of the graphite materials. This is a reasonable approximation, based on the results in Figure 3 which show nearly identical voltage responses for P5, P10, and P15 graphite powders at slow rates (C/10), and only small differences for the M3 material. The other parameters for this model are summarized in supplementary materials **Tables S2-S4** and **Figure S8**. Most of these values were either found in the literature or measured. Notably, two parameters were varied – the average particle size, and specific surface area of the graphite particles. It is important to note that the P2D model does not describe particle size distributions. However, the simpler description based on particle size and surface area is capable of providing relative comparisons for different particle sizes, which are well aligned with the experimental results that are reported here.

Two sets of simulations are presented here. First, a pair of simulations at a C-rate of 2C for two graphite materials with only the particle size varied (1 μm and 30 μm), and the SSA held to a constant value (3.52×10^6 1/m or 1.6 m^2/g), corresponding to P5 graphite, to test the effect of

particle size alone in the absence of other variables changing. The Butler-Volmer reaction rate was set to 5×10^{-10} $\frac{m^{2.5}}{mol^{0.5}s}$ to reduce effects of sluggish interface kinetics and simplify analysis. The second set of simulations varied both particle size and specific surface area simultaneously, which is more representative of real systems, as particle size and specific surface area are correlated. The particles were modeled as "flakes", meaning that the diffusion problem in the particle dimension was solved in cartesian coordinates (as compared to spherical coordinates in previous work on the same P5 graphite material system), to match the morphology of the graphite (**Figure 2**). In this set of simulations, several particle sizes were used; specifically, either the D_{50} or D_{90} particle diameter was used for P5 (6.5 μm or 12.2 μm), P10 (9.6 μm or 19.3 μm) and P15 (14.6 μm or 35.3 μm). The surface areas used were 1.6 m^2/g, 1.1 m^2/g and 1.0 m^2/g for P5, P10 and P15, respectively (**Table S5**). The Butler-Volmer reaction rate used was 1×10^{-10} $\frac{m^{2.5}}{mol^{0.5}s}$,[34, 35] and similar values have been used elsewhere (e.g. 1.7×10^{-10} $\frac{m^{2.5}}{mol^{0.5}s}$) [21]. Additionally, a simulation changing the particle surface area for P5 was conducted to examine the effect of surface area on plating onset. Plating onset was determined at any point in the electrode when

$$\eta_{\mathrm{Li}} = \phi_s - \phi_l = 0 \qquad (3)$$

where η_{Li} is the lithium overpotential ϕ_s is the solid phase potential and ϕ_l is the liquid phase potential. The surface interaction is directly related to the onset of lithium plating, as the intercalation fraction of the particle surface χ_{surf} directly defines the equilibrium potential $E_{eq}(\chi_{surf})$ and onset of lithium plating occurs. It can be rewritten as [34, 35]

$$E_{\mathrm{eq}} = -\eta \qquad (4)$$

where η is the surface overpotential. When Butler-Volmer kinetics are fast, and the overpotential is small compared to the equilibrium potential, plating occurs when $E_{eq} = 0$ V, which in turn occurs when the surface of particles is saturated with lithium $\chi_{surf} = 1$. When interface reaction kinetics are slower, plating onset will occur when $\chi_{surf} < 1$ due to the additional overpotential contribution. For materials with high electronic conductivity compared to ionic conductivity, this tends to occur near the graphite-separator interface.

3. Results and Discussion

Physical properties: The P series of samples used here (P5, P10 and P15) have the same microstructure and crystal phase except for the different particle size distributions. The results from X-ray diffraction (XRD) measurements (**Figure 1a)** show that the P series of samples have identical diffraction patterns, all reflections of which can be identified to the crystal graphite assuming a hexagonal crystal system with $P6_3/mmc$ symmetry, and the same d_{002} spacing of 3.354 Å. However, the graphite samples have different specific surface area (SSA), particle sizes and particle size distribution (PSD). The nitrogen sorption (**Figure 1b**) shows Type II isotherms for all samples, characteristics of nonporous or macroporous solids [48-50]. The results calculated from the BET method show that the SSA of P5 is ~1.6 m^2/g, decreases to ~ 1.1 m^2/g for P10 and ~1.0 m^2/g for P15. The laser scattering measurements (**Figure 1c**) demonstrate that P5 has the smallest average particle size (D_{50}) of ~6.5 μm, and narrowest PSD with 90% of particles below 12.2 μm (D_{90}). P10 has the medium D_{50} of ~9.6 μm and PSD with D_{90} of ~19.3 μm, while P15 has the largest average particle size (D_{50} = ~14.6 μm) and broadest PSD (D_{90} = 35.3 μm). The PSD can

be further confirmed by the SEM observations. **Figure 2** demonstrates that P series of graphite powders are composed of briquette-shaped particles (**Figure 2a** to **2c**). The particle size (width) of P5 was measured to be in range of 1-12 μm, while 4-21 μm for P10, and 3-34 μm for P15. This is consistent with the results from the PSD measurements via laser scattering. The M3 graphite has similar SSA and briquette shape as those of P10 and P15, but it has a larger average particle size of ~24.1 μm and appears to have gone through a shaping process due to its relatively rounded edges (**Figure 2d**). Furthermore, an additional reflection at ~ 43.2° might be assigned to (101) plane of a phase with the rhombohedral symmetry (**Figure 1a**), indicating that M3 has some hexagonal graphite sheets deformed after the shaping process [51]. The physical properties of all graphite samples are summarized in **Table S5**.

Battery performance: The particle size has little effect on the electrochemical behaviors of graphite anodes when the cells are lithiated/delithiated slowly or their state-of-charges (SOCs) are far away from the threshold value of the lithium plating onset. **Figure 3a** shows that the irreversible capacity loss (ICL) of the P series of graphite is 12-21% during the initial formation cycle, which is higher than that of M3 graphite (~8%). The higher ICL might be associated with the formation of thicker solid-electrolyte-interface (SEI) film, due to the higher edge area of briquette-like P series of graphite. However, all cells demonstrate an almost identical reversible capacity (delithiation capacity) of ~330 mAh/g and coulombic efficiency of ~99.2% after three formation cycles (**Figure 3b**). This implies that the morphology and particle size have little effect on the lithiation of graphite at low rates. Similar phenomena can be found at high rates with the lithiation

cut-off voltage of 10 mV. At the low rate of 0.1C, all cells demonstrate plateau-like voltage curves, which are gradually substituted by a sloping feature as the current density is elevated (**Figure 3c**). At a given rate, the voltage profiles of P10, P15 and M3 are almost overlapped, while P5 has slightly less overpotential. In addition, the capacity retention of all graphite gradually decreases as the current density applied increases (**Figure 3d**). At all rates, P10 and P15 have almost the same capacity retention as that of M3, considering the reasonable scope of experiment error. However, P5 demonstrates slightly higher capacity retention than P10, P15 and M3 at the rates ≥1C. Our previous work [16] showed that, when the cut-off voltage of the lithiation process is above 10 mV, the SOCs of cells are far below the threshold value of the onset of lithium plating, and the onset of Li plating plays a crucial role in the battery performance at high rates. It is therefore very challenging to discern the effect of particle size on the rate capability and durability of cells under fast charge.

Mitigated lithium plating: The particle size plays a crucial role in the onset of Li plating in graphite electrodes. After lithiation to various SOCs, the cells were relaxed for thirty minutes, and the voltage relaxation profiles (OCV) were recorded as a function of time (**Figure S1** and **S2**). The analysis (**Figure S3** and **S4**) of the voltage relaxation profile derivatives (dOCV) exhibits that the dOCV profiles of all graphite anodes decrease gradually and reach a new constant after various times when cells were lithiated to <80% SOCs (**Figure 4a**). After lithiated to 85% SOC, the dOCV curve obtained from the cell with P15 graphite exhibits an inflection point feature (**Figure 4b**), which is an indicative of the onset of Li plating, [41, 43] and this feature becomes more prominent at

high SOCs (**Figure 4c** and **4d**). The inflection point feature is observable on the dOCV profiles obtained at 90% for P10 (**Figure 4c**) and 95% for P5 (**Figure 4d**) respectively. This indicates that the onset of Li plating happens at a relative low SOC of 80-85% for P15, medium SOC of 85-90% for P10 and high SOC of 90-95% for P5. Apparently, reducing particle size can suppress the onset of Li plating in graphite electrodes. In addition, the dOCV peak shifts to the right with increasing particle size at a given SOC, indicating a larger amount of plated Li in the electrode with bigger particles [43]. Although having a different morphology of rounded shape, the onset of Li plating in the bigger M3 graphite occurs at 75-80% SOC, following the trend that, the larger the particle size, the lower the SOC at which the Li plating onset takes place. The analysis of the coulombic efficiency (CE) also confirms this (**Figure 4e**). A dramatic CE decrease can be observed on M3 graphite after 75% SOC, meanwhile this detriment to CE shifts to the right with decreasing particle size, to the extent that no significant CE drop is observed on P5 graphite until 90% SOC. A similar trend can be observed at the higher rate of 4C (**Figure S5** and **S6**). With the same test method and analysis procedure, the P5 graphite anode exhibits a Li plating onset at 50-60% SOC, 40-50% SOC for P10, 30-40% SOC for P15, and 20-30% SOC for M3 (**Table 1**) at 4C. The mitigated Li plating onset might be associated with the reduced diffusion length of Li ions in graphite phase and polarization of graphite electrodes with smaller particles, which will be discussed below.

The advantage of small graphite particles in suppressing the Li plating onset under fast charge application can be confirmed through microscopy observations on the electrodes before (**Figure S9**) and after (**Figure 5**, and **S10** to **S12**) rate tests. After lithiated to 90% SOCs at 2C, the cycled

P5 electrode has a quite clean surface (**Figure 5a**), while tremendous white agglomerates composed of numerous small particles are observable at the surface of cycled P10 (**Figure 5b**), P15 (**Figure 5c)** and M3 (**Figure 5d**) electrodes. The bigger the graphite particles, the more agglomerates are found at the surface of the electrodes. The energy dispersive X-ray spectroscopy (EDS) mapping over the cycled electrodes (**Figure 5e**, **S10** to **S12**) shows a representative white agglomerate that is composed of only the element oxygen (O), without carbon (C), fluorine (F), or phosphorous (P) elements. The absence of C, F and P elements excludes the possibilities that these white agglomerates are oxidized lithium salt from the residual electrolyte or SEI film formed at the surface of graphite electrodes during the lithiation/delithiation processes. It is highly possible that these white agglomerates come from plated Li metal particles, which were oxidized during the process of transferring samples to the SEM chamber. The SEM observations therefore indicate that, lithiated to 90% SOC at 2C, the onset of Li plating did not take place on the P5 graphite electrode, but it happened on other graphite electrodes, and the amount of plated Li increases alongside the increase of graphite particle size. This is consistent with the dOCV analysis, which concludes that, when the SOC is less than 90%, no Li dendrites are formed at the surface of the P5 graphite electrode, while dendrites formed in the P10, P15 and M3 graphite electrodes, and the amount of Li dendrites in the graphite electrodes increases with the increase of particle size. Results from both SEM observations and dOCV analysis suggest that small graphite particles can suppress the formation of Li dendrites in cells under fast charge applications.

Suppressed growth of plated Li particles: The particle size also has an important influence on

the growth of plated Li particles under fast charge application. Lithiated to 80% SOC at 4C, all cells exhibit stable voltage profiles during the initial 25 cycles (**Figure 6a** to **6d**). However, the dOCV analysis indicates that the onset of Li plating occurs in all graphite electrodes at 4C when cells are lithiated to >60% SOC (**Table 1**, Figure **S6** and **S13)**. For a given graphite, the dOCV peak shifts to the right along the cycling process, indicating the amount growth of plated Li in the electrode (**Figure S13**). Further, the cell with P15 graphite shows a voltage dip during the lithiation process when it proceeded to the twenty-sixth cycle and dramatically fluctuating voltage during following cycles (**Figure 6c**). The voltage dip is observed in the thirty-first cycle for P10 graphite (**Figure 6b**) and fortieth cycle for P5 graphite (**Figure 6a**). Similar to the Li plating onset, the M3 graphite electrode shows the voltage dip in the twenty-fifth cycle (**Figure 6d**), which is slightly earlier than for P15 graphite. Apparently, the emergence of the voltage dip is an indication that the amount of plated Li particles or their sizes at the surface of graphite electrode reaches a threshold value, above which the battery performance will show unstable potential. The mitigated emergence of a voltage dip implies that the smaller graphite particle can suppress the growth of plated Li particles under fast charging.

The suppressed growth of metallic Li particles can reduce the polarization of graphite electrodes, evidenced by the lower overpotential of smaller graphite at every cycle (**Figure 6a** to **6d**). In addition, the fast growth of Li dendrites has a significant influence on the successive intercalation/deintercalation processes in graphite electrodes. The delithiation capacity delivered by M3 dramatically drops from ~240 mAh/g to ~190 mAh/g during the initial 4 cycles, partially

recovers to ~220 mAh/g after 10 cycles, decreases gradually to ~210 mAh/g after 20 cycles, and greatly decreases to ~120 mAh/g after 35 cycles (**Figure 6e**). However, the delithiation capacity of P5 gradually decreases from ~250 mAh/g to ~230 mAh/g during the first 25 cycles and drops to ~200 mAh/g after 35 cycles. The evolution of delithiation capacities of P10 and P15 exhibits the same trend as that of P5 but drops more quickly during the initial 30 cycles. The same trend can be observed on the coulombic efficiency (**Figure 6f**). Therefore, the small particles can not only increase the capacity via facilitating intercalation/deintercalation processes, but also prolong the cycle life of cells through suppressing plated Li particle growth under fast charge. It is worth noting that the particle size has an effect on both Li plating and formation of SEI film at the surface of graphite. Both can affect the electrochemical performance of graphite anodes, especially under fast charge operations with high current densities. With graphite samples studied here, the thickness difference of SEI films at the surface of various graphite particles might be negligible and Li plating has a more prominent effect on the cycling performance of graphite anodes. If it is thick, the high resistance of the SEI film might have a dominant effect on the electrochemical behaviors of graphite anodes. It has been reported that, when the particle size is too small, the increased surface area facilitates the formation of thick SEI film[39, 52], significantly increases the high resistance, and has an adverse effect on the cycle efficiency and durability of cells[39, 53, 54].

Mechanism study: Li plating is thermodynamically possible when the surface of a single graphite particle at any location the electrode is saturated with lithium ($\chi_{surf} = 1$). It is, therefore, very important to understand how intercalation varies as a function of position in the electrode and

across the thickness of the particles at each point in the electrode. **Figure 7** shows the evolution of the surface intercalation fraction (χ_{surf}) in the particles (**Figure 7a** and **7b**) and the average intercalation in the particles (χ_{avg}) (**Figure 7c** and **7d**) as a function of position in the electrode and as a function of cell SOC (i.e., time). The comparison between a very small particle (**Figure 7a**) and a relatively bigger particle (**Figure 7b**) demonstrates how the diffusion limitations through the particle changes intercalation, for the case where the SSA is held constant. The surface intercalation for smaller particles (**Figure 7a**) tends to be lower at any given cell SOC (increasing from black to red lines) as compared to bigger particles (**Figure 7b**). This indicates that plating will occur at lower SOCs for bigger particles, due to the gradients in intercalation through the particle thickness (**Figure 7c** and **7d**). For small enough particles at a given C-rate, $\chi_{surf} \approx \chi_{avg}$ (**Figure 7a** and **7c**) as there is no transport limitation through the particles. However, for bigger particles at high C-rates, there is not enough time for lithium to fully intercalate through the particles and $\chi_{surf} > \chi_{avg}$ (**Figure 7b** and **7d**). Here the surface intercalation fraction (χ_{surf}) will increase faster (**Figure 7b**), compared to the small particle case (**Figure 7a**), as the total charge in the cell is fixed at any given time. This can be related to onset of plating by observing the χ_{surf}, χ_{avg}, E_{eq}, and η_{Li} at the time of plating onset as a function of position in the electrode (**Figure S14**). As the surface intercalation approaches saturation ($\chi_{surf} = 1$) at the graphite-separator interface (**Figure S14a**) the equilibrium potential approaches 0 V (**Figure S14c**) and the lithium overpotential approaches 0 V (**Figure S14d**) in the same location. For a 1μm particle, this occurs while $\chi_{surf} \approx \chi_{avg}$, whereas for the 30 μm particle this occurs when $\chi_{surf} > \chi_{avg}$ (**Figure S14a** and **S14b**), resulting in plating onset at lower cell SOC for the bigger particle.

Simulations of P5, P10 and P15 graphite were conducted at 2C and 4C corresponding to the experiments conducted herein (**Table 1**). In these simulations, the measured SSA of the particles and electrode thickness and porosity matched those in the corresponding experiments. However, the P2D finite element model does not allow for particle range distributions, so two simulations were run corresponding to each material – one for the D_{50} particle size and one for the D_{90} particle size. The cell SOC at the onset of plating is summarized for each of these cases in **Table 1**. Generally, D_{50} gives a closer approximation to the experimentally measured results than D_{90}. The simulated plating onset is in agreement with experimental ranges for P5, P10 and P15 at 2C, as well as P5 at 4C. However, D_{50} simulation overestimates the SOC at plating onset for P10 and P15 at 4C, while D_{90} simulation underestimates it for all cases, except for P5 in which case it falls in the expected range. For the present analysis, the increased surface area does not change the plating threshold substantially, as can be observed by comparing the capacity for different particle sizes both including the surface area change with particle size and keeping the surface area the same for different particle sizes (**Figure S15)**. This effect may be small because the contribution surface reaction to accelerated plating onset is negligible. This effect on surface reaction kinetics may play a role in accelerating plating onset, but it is difficult to determine whether this is the case from a computational standpoint because the reaction rate has differed by over an order of magnitude between studies in the literature[34, 35]. It is noteworthy that our previous work[34, 35] has suggested the "reaction inhomogeneity" effect is dominant relative to the role of kinetics in plating onset for graphite electrodes at fast rates, at least in the range of reported literature values for reaction kinetics parameters.

The voltage curves from experiments indicate lower voltages in larger particle size graphite materials (**Figure S16a**), and higher resistance as indicated by impedance measurements (**Figure S16b** and **Table S6**). Simulations show a similar trend of lower voltage at a given SOC for increasing particle size (**Figure S16c**), and these trends correlate to more accelerated lithium plating at high rates for larger particles size (**Figure S16d**). Although reasonable estimates of plating onset were observed (**Table 1**), the predicted voltages in the simulations do not precisely match the experiments. This appears to be true to challenges that are associated with the relatively larger number of parameters in the electrochemical model, compared to the relatively limited number of experimental data sets used for fitting (cell voltage, plating onset). These effects could be produced empirically by varying impedance in one or more locations (e.g., due to SEI on the particles or the Li metal electrode, etc.). However, this type of forced fit without direct experimental calibration is not physically meaningful and does not provide any additional insight into understanding the impact of particle size on Li plating onset, which is the primary focus of the current study.

4. **Conclusion**

The effect of particle size on the battery performance of graphite electrodes under fast charge operations was elucidated here. The analysis of the voltage relaxation profiles reveals that the Li plating onset does not happen in the electrodes with small P5 graphite particles (D_{50} of 6.5 μm) until lithiated to 95% SOC at 2C. Electrodes with bigger particles exhibited the occurrence of Li plating at earlier SOCs at high rates. Observations from electron microscopy also corroborated the

presence of plated Li in electrodes with bigger graphite particles, and absence in P5 graphite electrode. In addition, the small particles also have the capability to suppress the growth of metallic Li particles plated in the graphite electrodes under fast charge. The simulated results manifest the dependence of Li plate onset on the particle size of graphite and reveal that the relatively lower surficial Li^+ concentration in small particles can significantly reduce the overpotential in the graphite electrodes and thus mitigate the onset of Li plating. These findings make the diffusion of lithium within an individual graphite particle as important as the mass transport across the electrode at high rates. Thus, the achievements obtained here are of both scientific and practical significance in the design and fabrication of anode materials for fast charging LIBs.

Acknowledgments

This material is based upon work supported by the U.S. Department of Energy's Office on Energy Efficiency and Renewable Energy (EERE) under the Advanced Manufacturing Office, award number DE-EE0009111. The authors are also grateful for the graphite products from Phillips 66.

References

1. H. Zhang, Y. Yang, D. Ren, L. Wang and X. He, *Energy Storage Mater.*, 2021, **36**, 147-170.
2. J. Li, J. Fleetwood, W. B. Hawley and W. Kays, *Chem. Rev.*, 2021, **122**, 903-956.
3. K. G. Gallagher, S. E. Trask, C. Bauer, T. Woehrle, S. F. Lux, M. Tschech, P. Lamp, B. J. Polzin, S. Ha and B. Long, *J. Electrochem. Soc.*, 2015, **163**, A138.
4. W. Cai, Y.-X. Yao, G.-L. Zhu, C. Yan, L.-L. Jiang, C. He, J.-Q. Huang and Q. Zhang, *Chem. Soc. Rev.*, 2020, **49**, 3806-3833.
5. Y. Chen, Y. Kang, Y. Zhao, L. Wang, J. Liu, Y. Li, Z. Liang, X. He, X. Li and N. Tavajohi, *J. Energy Chem.*, 2021, **59**, 83-99.
6. A. Tomaszewska, Z. Chu, X. Feng, S. O'kane, X. Liu, J. Chen, C. Ji, E. Endler, R. Li and L. Liu, *ETransportation*, 2019, **1**, 100011.
7. A. M. Colclasure, A. R. Dunlop, S. E. Trask, B. J. Polzin, A. N. Jansen and K. Smith, *J. Electrochem. Soc.*, 2019, **166**, A1412.
8. X. Lin, K. Khosravinia, X. Hu, J. Li and W. Lu, *Prog. Energy Combust. Sci.*, 2021, **87**, 100953.
9. Y. Liu, Y. Zhu and Y. Cui, *Nat. Energy*, 2019, **4**, 540-550.
10. H. Wang, Y. Zhu, S. C. Kim, A. Pei, Y. Li, D. T. Boyle, H. Wang, Z. Zhang, Y. Ye and W. Huang, *Proc. Natl. Acad. Sci. U.S.A*, 2020, **117**, 29453-29461.
11. M.-T. F. Rodrigues, K. Kalaga, S. E. Trask, D. W. Dees, I. A. Shkrob and D. P. Abraham, *J. Electrochem. Soc.*, 2019, **166**, A996.
12. P. Zhang, T. Yuan, Y. Pang, C. Peng, J. Yang, Z.-F. Ma and S. Zheng, *J. Electrochem. Soc.*, 2019, **166**, A5489.
13. B. S. Vishnugopi, A. Verma and P. P. Mukherjee, *J. Electrochem. Soc.*, 2020, **167**, 090508.
14. Z. Q. Chen, D. L. Danilov, L. H. J. Raijmakers, K. Chayambuka, M. Jiang, L. Zhou, J. Zhou, R. A. Eichel and P. H. L. Notten, *J. Power Sources*, 2021, **509**, 230345.
15. D. S. Hall, A. Eldesoky, E. Logan, E. M. Tonita, X. Ma and J. Dahn, *J. Electrochem. Soc.*, 2018, **165**, A2365.
16. J. Yang, Y. Li, A. Mijailovic, G. Wang, J. Xiong, K. Mathew, W. Lu, B. W. Sheldon and Q. Wu, *J. Mater. Chem. A*, 2022, **10**, 12114-12124.
17. S. Kalnaus, K. Livingston, W. B. Hawley, H. Wang and J. Li, *J Energy Storage*, 2021, **44**, 103582.
18. A. Shodiev, F. M. Zanotto, J. Yu, M. Chouchane, J. Li and A. A. Franco, *Energy Storage Mater.*, 2022, **49**, 268-277.
19. R. Amin, B. Delattre, A. P. Tomsia and Y.-M. Chiang, *ACS Appl. Energy Mater.*, 2018, **1**, 4976-4981.
20. J. Billaud, F. Bouville, T. Magrini, C. Villevieille and A. R. Studart, *Nat. Energy*, 2016, **1**, 1-6.
21. K.-H. Chen, M. J. Namkoong, V. Goel, C. Yang, S. Kazemiabnavi, S. Mortuza, E. Kazyak, J. Mazumder, K. Thornton and J. Sakamoto, *J. Power Sources*, 2020, **471**, 228475.

22. J. B. Habedank, J. Kriegler and M. F. Zaeh, *J. Electrochem. Soc.*, 2019, **166**, A3940.
23. L. Li, R. M. Erb, J. Wang, J. Wang and Y. M. Chiang, *Adv. Energy Mater.*, 2019, **9**, 1802472.
24. D. Parikh and J. L. Li, *Carbon*, 2022, **196**, 525-531.
25. W. Xie, X. Liu, R. He, Y. Li, X. Gao, X. Li, Z. Peng, S. Feng, X. Feng and S. Yang, *J Energy Storage*, 2020, **32**, 101837.
26. M. Weiss, R. Ruess, J. Kasnatscheew, Y. Levartovsky, N. R. Levy, P. Minnmann, L. Stolz, T. Waldmann, M. Wohlfahrt-Mehrens and D. Aurbach, *Adv. Energy Mater.*, 2021, **11**, 2101126.
27. S. J. An, J. Li, C. Daniel, D. Mohanty, S. Nagpure and D. L. Wood III, *Carbon*, 2016, **105**, 52-76.
28. T. Waldmann, B.-I. Hogg, M. Kasper, S. Grolleau, C. G. Couceiro, K. Trad, B. P. Matadi and M. Wohlfahrt-Mehrens, *J. Electrochem. Soc.*, 2016, **163**, A1232.
29. D. S. Kim, Y. E. Kim and H. Kim, *J. Power Sources*, 2019, **422**, 18-24.
30. N. Kim, S. Chae, J. Ma, M. Ko and J. Cho, *Nat. Commun.*, 2017, **8**, 1-10.
31. Z. Ma, Y. Zhuang, Y. Deng, X. Song, X. Zuo, X. Xiao and J. Nan, *J. Power Sources*, 2018, **376**, 91-99.
32. H. Li and H. Zhou, *ChemComm*, 2012, **48**, 1201-1217.
33. J. Kim, S. M. N. Jeghan and G. Lee, *Microporous Mesoporous Mater.*, 2020, **305**, 110325.
34. A. S. Mijailovic, G. Y. Wang, Y. J. Li, J. Yang, W. Q. Lu, Q. L. Wu and B. W. Sheldon, *J. Electrochem. Soc.*, 2022, **169**, 060529.
35. A. S. Mijailovic, G. Y. Wang, M. Luo, W. Q. Lu, Q. L. Wu and B. W. Sheldon, *J. Electrochem. Soc.*, 2023, **170**, 070508.
36. K. Zaghib, X. Song, A. Guerfi, R. Kostecki and K. Kinoshita, *J. Power Sources*, 2003, **124**, 505-512.
37. H. R. Xia, W. Zhang, S. K. Cao and X. D. Chen, *Acs Nano*, 2022, **16**, 8525-8530.
38. W. Xu, C. Welty, M. R. Peterson, J. A. Read and N. P. Stadie, *J. Electrochem. Soc.*, 2022, **169**, 010531.
39. K. Zaghib, F. Brochu, A. Guerfi and K. Kinoshita, *J. Power Sources*, 2001, **103**, 140-146.
40. Q. Liu, T. Zhang, C. Bindra, J. Fischer and J. Josefowicz, *J. Power Sources*, 1997, **68**, 287-290.
41. S. Schindler, M. Bauer, M. Petzl and M. A. Danzer, *J. Power Sources*, 2016, **304**, 170-180.
42. X.-G. Yang, S. Ge, T. Liu, Y. Leng and C.-Y. Wang, *J. Power Sources*, 2018, **395**, 251-261.
43. Z. M. Konz, E. J. McShane and B. D. McCloskey, *ACS Energy Letters*, 2020, **5**, 1750-1757.
44. U. R. Koleti, T. Q. Dinh and J. Marco, *J. Power Sources*, 2020, **451**, 227798.
45. D. Parikh, T. Christensen and J. Li, *J. Power Sources*, 2020, **474**, 228601.
46. J. Landesfeind, J. Hattendorff, A. Ehrl, W. A. Wall and H. A. Gasteiger, *J. Electrochem. Soc.*, 2016, **163**, A1373.
47. A. Nyman, M. Behm and G. Lindbergh, *Electrochim. Acta*, 2008, **53**, 6356-6365.

48. Z. A. ALOthman, *Materials*, 2012, **5**, 2874-2902.
49. S. Lowell, J. E. Shields, M. A. Thomas and M. Thommes, *Characterization of porous solids and powders: surface area, pore size and density*, Springer Dordrecht, 2010.
50. J. Broekhoff, in *Studies in surface science and catalysis*, eds. B. Delmon, P. Grange, P. Jacobs and G. Poncelet, Elsevier, Louvain-la-Neuve, 1979, vol. 3, ch. Mesopore determination from nitrogen sorption isotherms: Fundamentals, scope, limitations, pp. 663-684.
51. C. Monteserin, M. Blanco, E. Aranzabe, A. Aranzabe, J. M. Laza, A. Larranaga-Varga and J. L. Vilas, *Polymers*, 2017, **9**, 16.
52. Y. S. Park and S. M. Lee, *Electrochim. Acta*, 2009, **54**, 3339-3343.
53. L. Blaubaum, F. Roder, C. Nowak, H. S. Chan, A. Kwade and U. Krewer, *Chemelectrochem*, 2020, **7**, 4755-4766.
54. H. Buqa, D. Goers, M. Holzapfel, M. E. Spahr and P. Novak, *J. Electrochem. Soc.*, 2005, **152**, A474-A481.

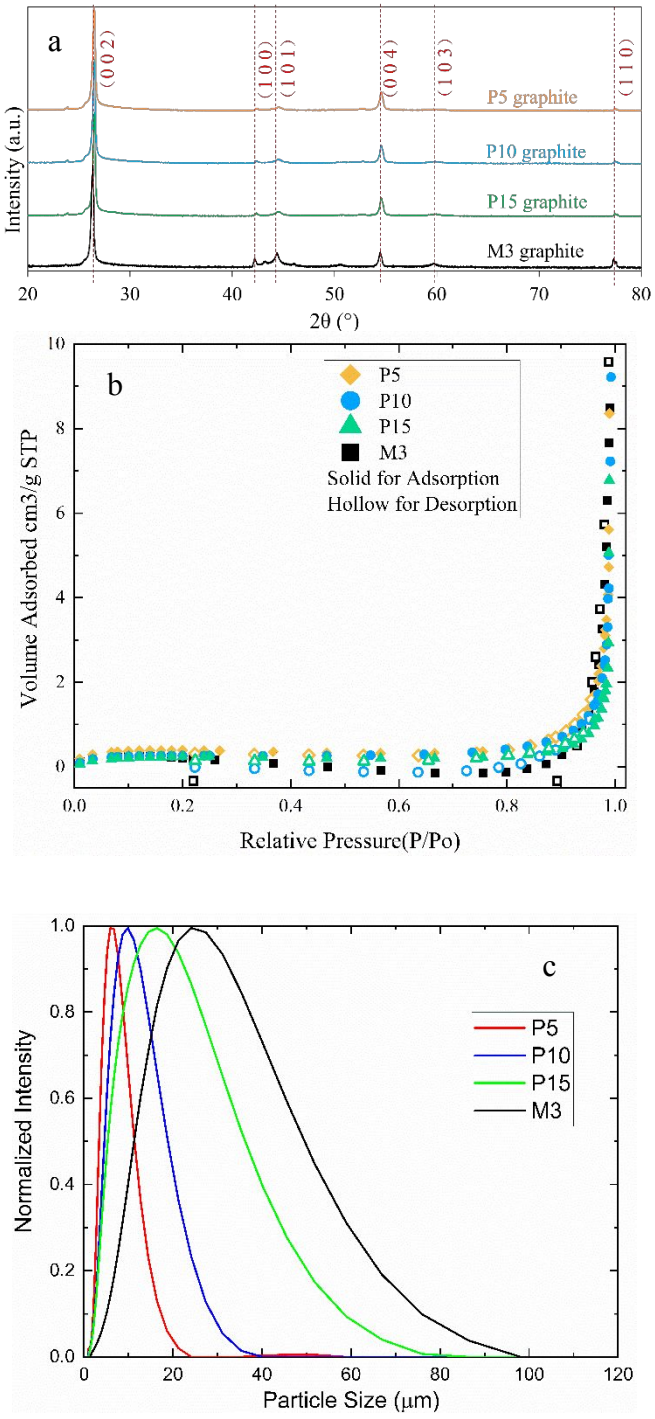

Figure 1. XRD patterns (a), nitrogen sorption isotherm plots (b) and particle size intensity distribution curves (c) of graphite samples. All reflections could be identified to graphite crystal and indexed by assuming a hexagonal crystal system with $P6_3/mmc$ symmetry.

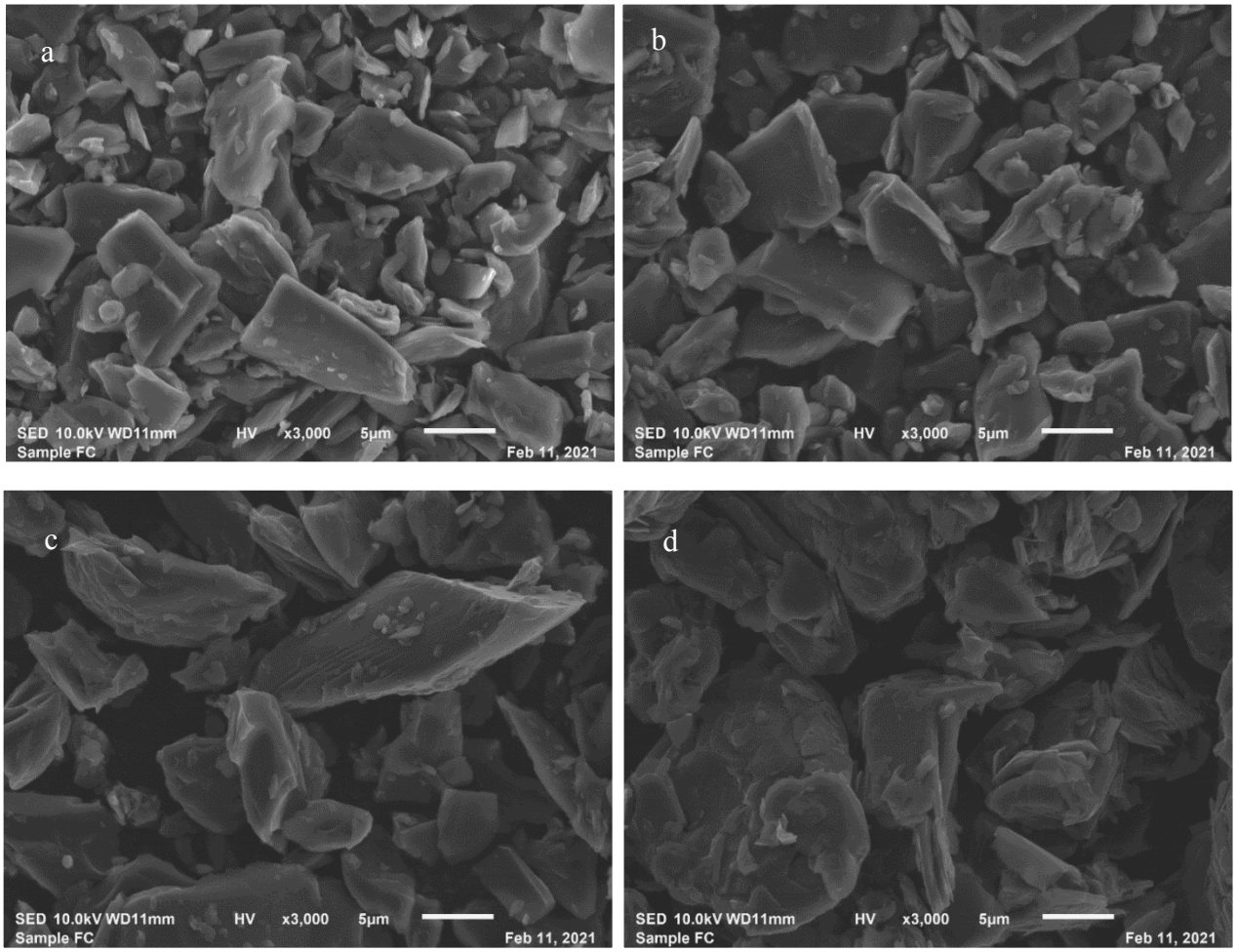

Figure 2. The SEM images of P5 (a), P10 (b), P15 (c) and M3 (d) graphite. P5-P15 graphite powders (a-c) exhibit irregular morphology with sharp edges, while rounded shape is observed on M3 graphite (d).

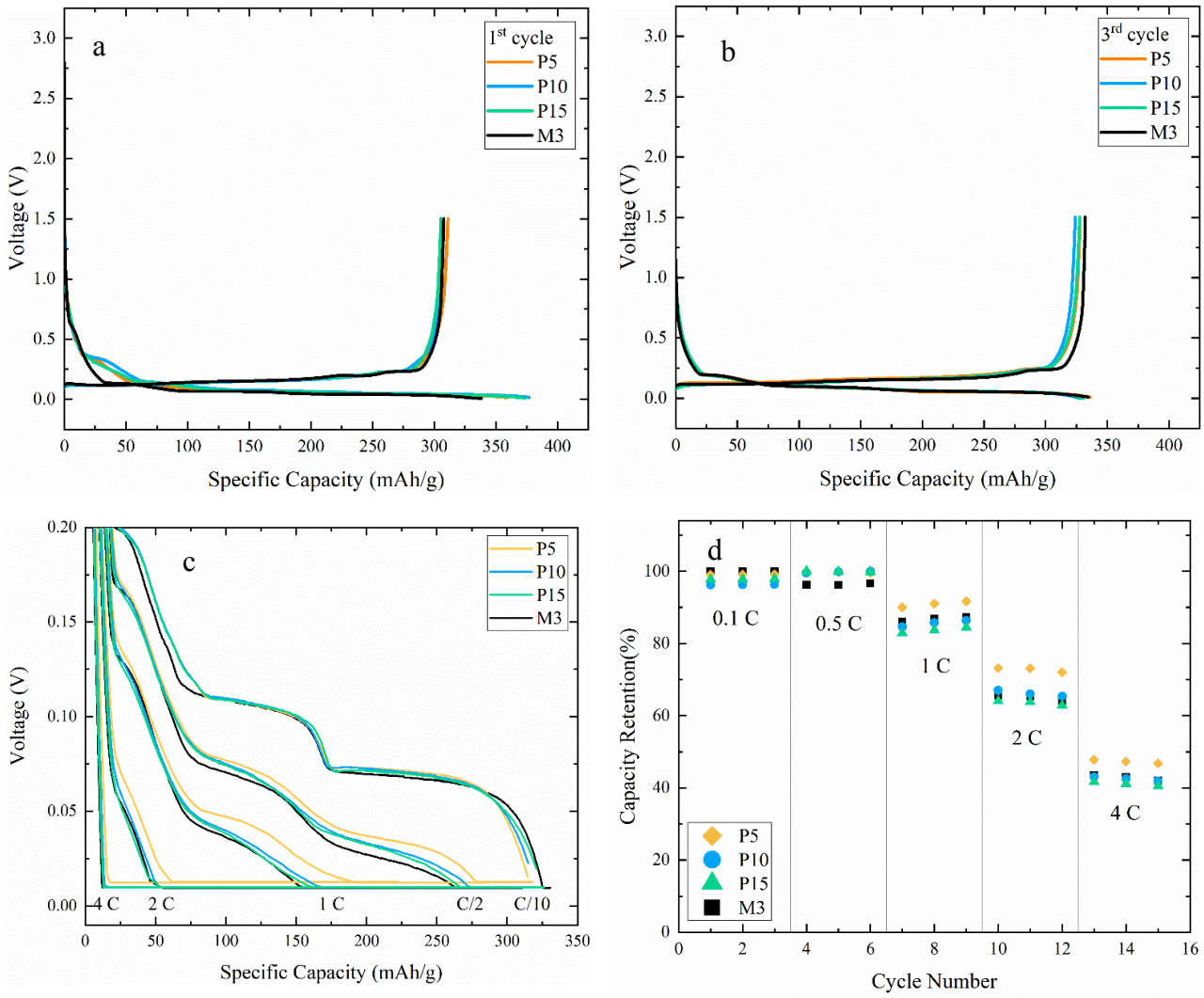

Figure 3. Voltage profiles of cells with various graphite electrodes during the first (a) and third (b) formation cycles. The voltage profiles (c) in the lithiation process at different rates and the rate capability (d) of cells with various graphite electrodes. The voltage profiles were extracted from the third lithiation process at every rate.

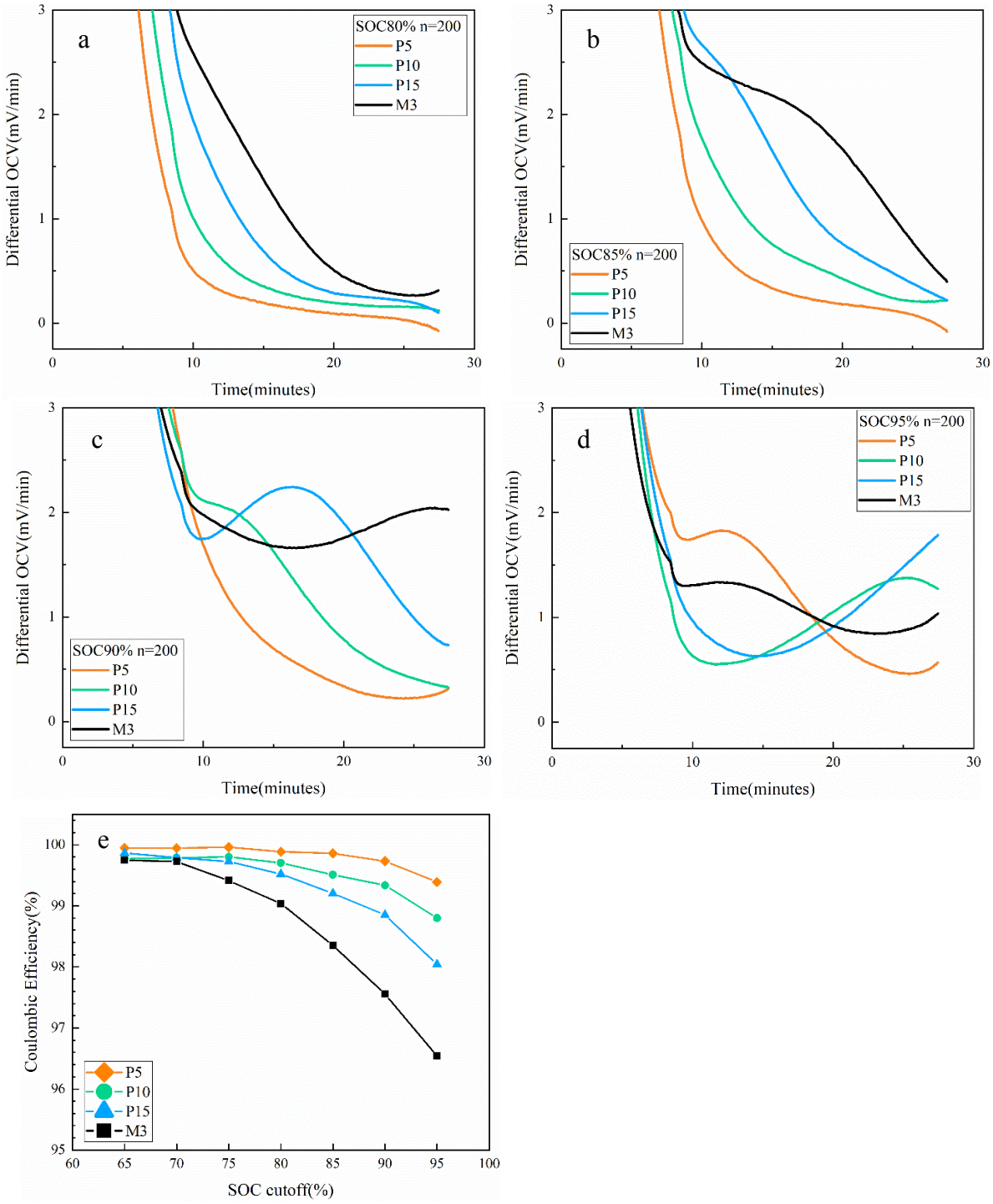

Figure 4. The comparison of differential OCV profiles of cells with different graphite anodes discharged to 80% (a), 85% (b), 90% (c) and 95% (d) at 2C, and the Coulombic efficiency (e) of cells as function of SOC.

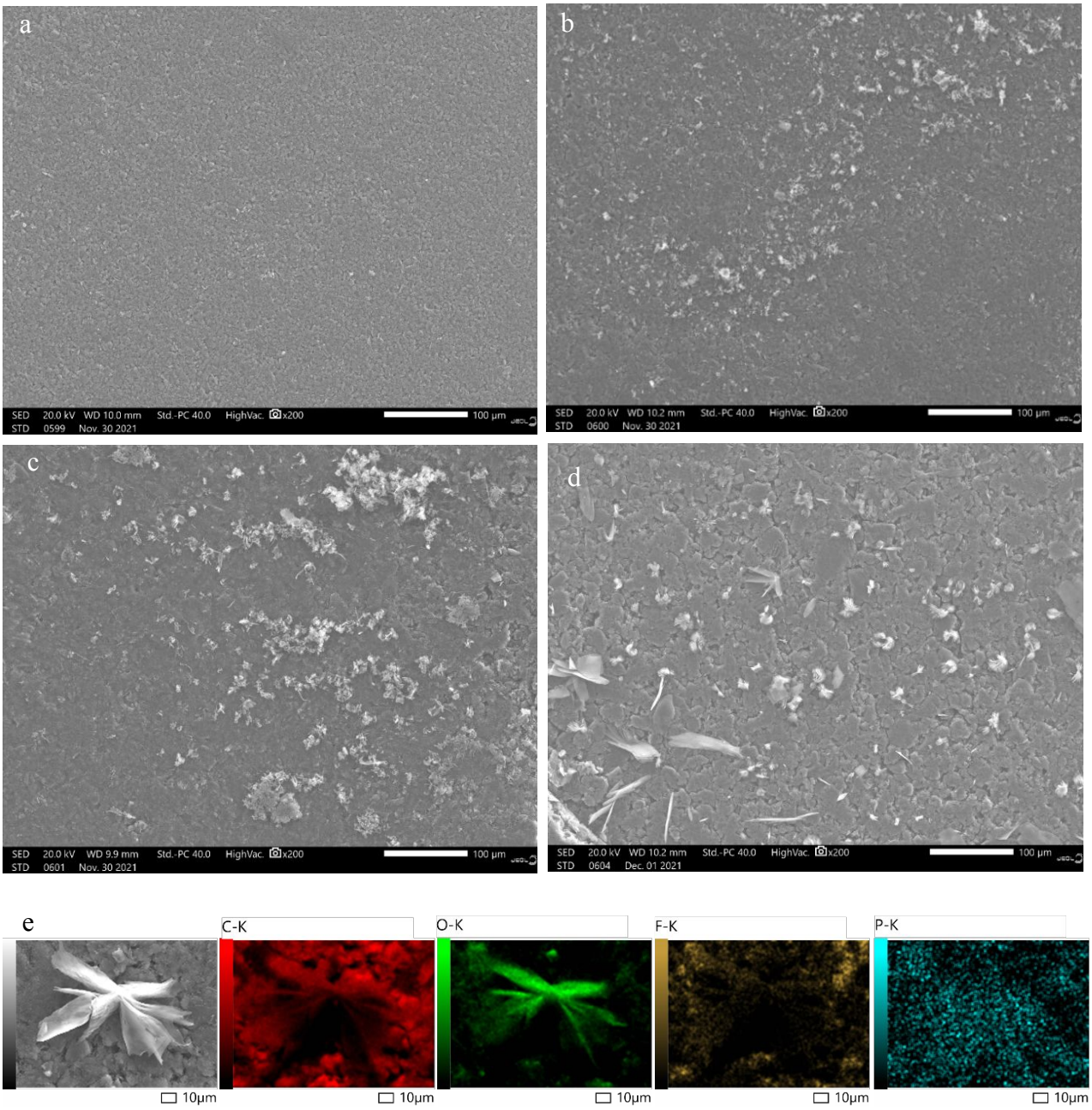

Figure 5. SEM images of cycled electrodes with P5 (a), P10 (b), P15 (c) and M3 (d) graphite. Before disassembly, all cells underwent rate tests lithiated to 90% SOC at 2C and were charged to 1.5 V. EDS mapping (e) collected on the cycled M3 electrode.

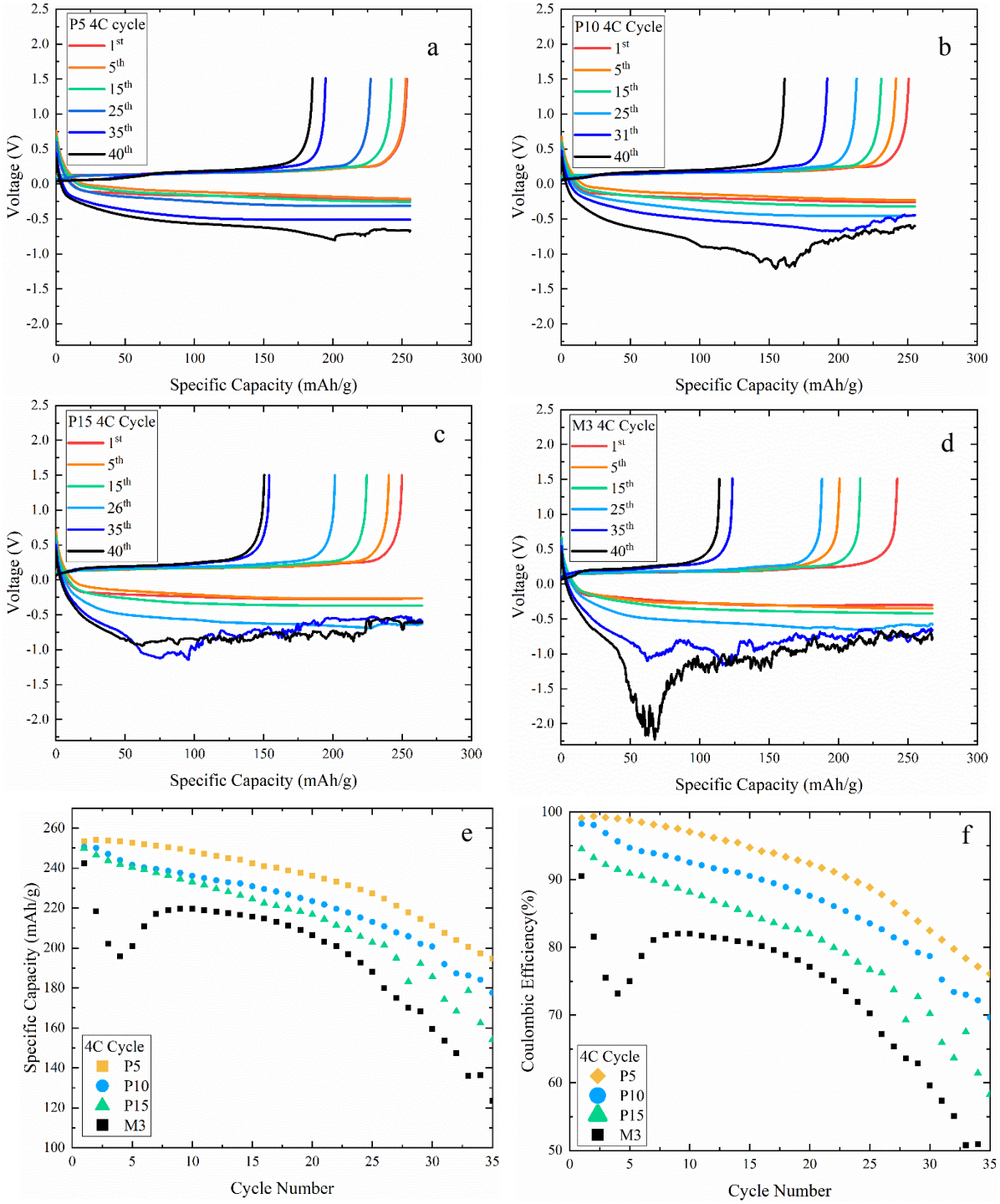

Figure 6. Voltage profiles (a-d), specific charge capacity (e), and coulombic efficiency (f) of cells with P5 (a), P10 (b), P15 (c) and M3 (d) graphite electrodes during the cycle tests. The current density applied to all cells was 4C.

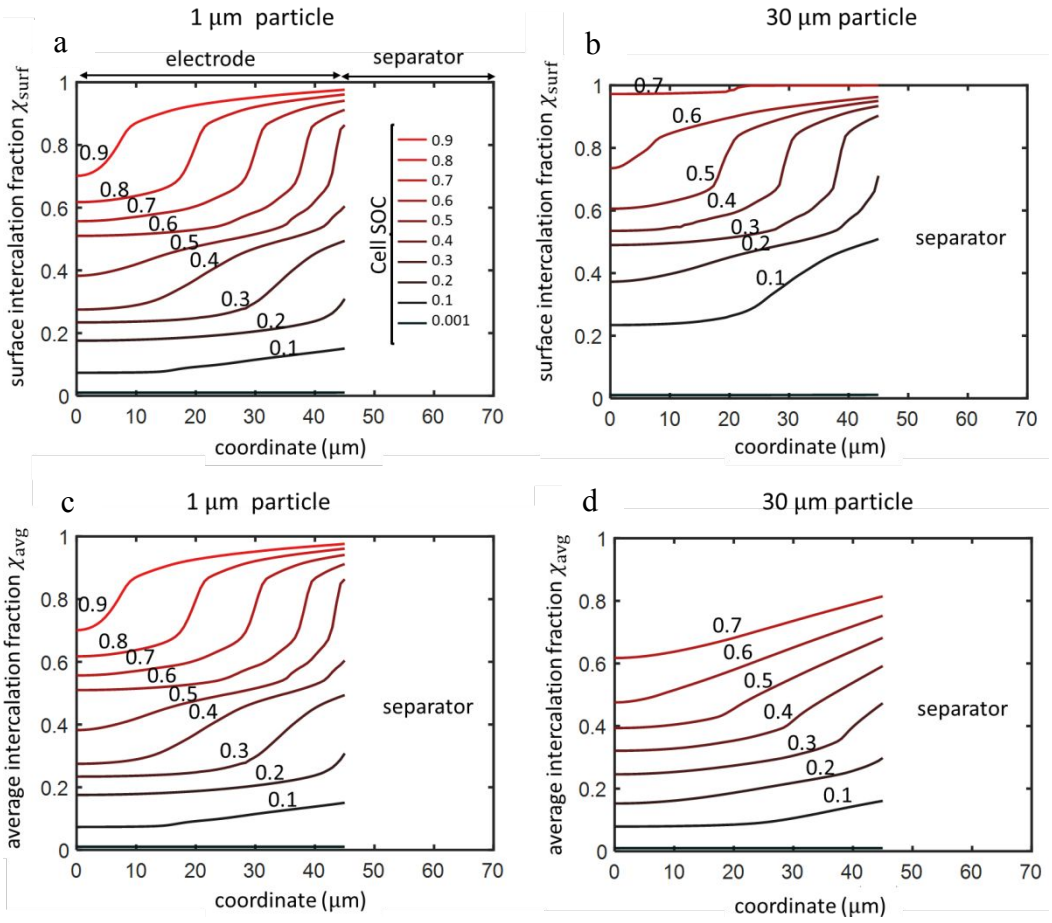

Figure 7. Surface intercalation fraction (χ_{surf}) as a function of coordinate for (a) 1μm particle and (b) 30 μm particle and average intercalation fraction (χ_{avg}) as a function of coordinate for (c) 1μm particle and (d) 30 μm particle. Colors from black to red represent increasing cell SOC, and cell SOC is indicated on the top of each trace. Electrodes here have a 45 μm thickness and 35% porosity.

Table 1. SOCs corresponding to Li plating onset at various rates

Rate	2C				4C			
Graphite electrode	Electrode thickness	Theoretical prediction (D50)*	Theoretical prediction (D90)**	Experimental value	Electrode thickness	Theoretical prediction (D50)*	Theoretical prediction (D90)**	Experimental value
P5	45	90%	88%	90-95%	53	55%	51%	50-60%
P10	47	87%	81%	85-90%	54	51%	36%	40-50%
P15	48	84%	54%	80-85%	54	45%	13%	30-40%

* The D50 particle sizes measured from graphite samples were used as inputs of the theoretical models

** The D90 particle sized measured from graphite samples were used as inputs of the theoretical models